

# Soot Formation in the Pyrolysis of Benzene, Methylbenzene, and Ethylbenzene in Shock Waves

G. L. Agafonov, P. A. Vlasov, and V. N. Smirnov

*Semenov Institute of Chemical Physics, Russian Academy of Sciences, Moscow, 119991 Russia*

*e-mail: iz@chph.ras.ru*

Received May 20, 2010

**Abstract**—Soot formation in the pyrolysis of benzene, methylbenzene, and ethylbenzene and in the oxidative pyrolysis of benzene in shock waves has been investigated using an absorption–emission technique. Even in the presence of small amounts of oxygen, soot formation in the pyrolysis of these hydrocarbons is accompanied by a decrease in the temperature of the reacting mixture. The soot yield has been measured as a function of temperature over wide initial reactant concentration ranges. A new, larger value was obtained for the coefficient of light absorption by soot particles at a wavelength of 632.8 nm. A revised, substantially modified kinetic model is suggested for soot formation. This model has been verified against experimental data available from the literature on the time profiles of the concentrations of some key components at the early stages of pyrolysis and oxidation of various hydrocarbons in a wide range of process conditions. The model reproduces fairly well the time dependences of the soot yield and soot particle temperature measured in this study for benzene, methylbenzene, and ethylbenzene pyrolysis.

**DOI:** 10.1134/S0023158411030013

The formation of soot particles in hydrocarbon pyrolysis and oxidation is a complicated multistep process that includes numerous competing homogeneous and heterogeneous reactions, namely, oxidation, thermal decomposition, and the formation of new chemical bonds, which yield the most stable hydrocarbons under the given conditions [1]. Although soot formation has been investigated both experimentally and theoretically, there are some unclear issues about this process, including the chemical structure of the hydrocarbons forming at the earliest soot formation stages [1–9]. Most studies on soot formation have been carried out using various types of flames. Note, however, that soot formation in flames can be investigated only in rather narrow concentration and temperature ranges because of the problem of maintaining self-sustaining combustion. For example, the oxidizer concentration cannot be below a certain level, so this process is rather specific. An additional complicating factor in soot formation in flames arises from transport processes, which cause temperature and composition nonuniformities. None of these complications is encountered in measurements in reflected shock waves. Under shock wave conditions, the temperature and density of the reaction mixture remain practically constant over 1–2 ms and transport processes do not play any significant role. Thus, a shock tube provides a means to study soot formation in much wider ranges of conditions without significant complicating factors. This substantially facilitates data

interpretation and data comparison to predictions of kinetic soot formation models [10–12].

The most efficient approach to testing the predictive potential of soot formation mechanisms is to compare experimental and calculated data for different hydrocarbons and for wide ranges of conditions.

Here, we report an experimental study of soot formation in benzene, methylbenzene (toluene), and ethylbenzene pyrolysis behind reflected shock waves and a detailed kinetic modeling of soot formation in terms of our kinetic scheme of the process. The main purpose of this study is to elucidate the soot nucleation mechanism. According to our soot formation model, the above hydrocarbons play the role of primary units in the formation of soot nuclei. The pyrolysis data reported here for these hydrocarbons minimize the uncertainties in the existing mechanisms of the formation of aromatic hydrocarbons from smaller hydrocarbon fragments in the gas phase at relatively high temperatures. The systems examined have aromatic rings from the very beginning of the process, and these rings serve as nucleators for the formation of progressively larger aromatic fragments, which eventually make up soot nuclei.

## EXPERIMENTAL

### *Shock Tube*

A stainless steel shock tube was used in our experiments (inner diameter of 75 mm, low-pressure section length of 1.5 m, high-pressure section length of 3.2 m).

The low-pressure section was evacuated with two 2-NVR-5D fore pumps to a residual pressure of  $10^{-2}$  Torr and with an NVDS-100 oil diffusion pump to  $10^{-3}$  Torr. For attaining a higher vacuum, the system was equipped with two liquid-nitrogen traps. The residual pressure was monitored with a VIT-2 ionization-thermocouple vacuum gage. The high-pressure section was evacuated with a 2-NVR fore pump through a liquid-nitrogen trap to a residual pressure of 0.1 Torr. Air leakage into the low-pressure section did not exceed  $10^{-4}$  Torr/min. Before each experiment, the low-pressure section was purged two times with argon to be used in mixture preparation with intermediate pumping to  $10^{-1}$  Torr.

The parameters of the gas behind the incident and reflected shock waves were calculated from the initial pressure, mixture composition, and incident shock wave velocity within the theory of ideal flow in a shock tube [13]. The velocity of the incident shock wave was measured on two bases using three pressure sensors placed in series ( $D_1$ ,  $D_2$ ,  $D_3$ ). The distances between  $D_1$  and  $D_2$  was 528 mm; the distance between  $D_2$  and  $D_3$ , 281 mm. The most remote sensor,  $D_3$ , was positioned 40 mm from the set of optical windows in the body of the shock tube. The pressure sensors, with a sensing element 1 mm in diameter, were made from piezoceramics (lead zirconate titanate) and were coated with a protective wax layer 0.3–0.5 mm in thickness. They were mounted flush with the inner wall of the shock tube. The signals generated by the sensing elements of the pressure sensors during the passage of the shock wave were inputted into emitter followers and were then directed to G5-15 generating amplifiers and Ch3-33 frequency meters operating in the time measurement mode.

The shock wave was generated by a spontaneous burst of one or several piled aluminum diaphragms 0.05–0.2 mm in thickness, depending on what conditions were to be established behind the incident or reflected shock wave. The diaphragms were placed in a special-purpose holder between the high- and low-pressure sections, where they were secured with two vacuum rubber rings (one on either side) 80 mm in diameter, 5 mm in width, and 4 mm in thickness.

The driver gas was helium. The diaphragms of the above-specified thickness ruptured at a nearly the same driver gas pressure. For this reason, when it was necessary to vary the temperature behind the incident or reflected shock wave at an approximately constant density of the shock-compressed gas, the driver gas was a helium–air mixture with a prescribed air content of up to 50%: the lower the temperature to be established behind the shock wave, the higher the percentage of air to be introduced in to the driver gas mixture.

#### *Preparation and Composition Control of the Working Gas Mixture in the Shock Tube*

The mixtures to be examined were composed manometrically and were stored in lightproof bottles. The components were benzene (reagent grade), toluene (reagent grade), ethylbenzene (reagent grade), and oxygen (99.0%). The diluent gas was argon (99.998%). The mixtures were prepared as follows. A liquid component (benzene, toluene, or ethylbenzene) was syringed into a trap and was frozen with liquid nitrogen. The trap was evacuated, the flask with liquid nitrogen was removed, and pumping was continued until the liquid began to evaporate intensively. Pumping was then stopped, and the liquid was allowed to evaporate into a pre-evacuated bottle until the preset pressure was reached. A preset amount of oxygen was added if necessary. Thereafter, argon was admitted into the bottle up to a pressure of 600 Torr, the valve was closed, and the bottle was left standing for 1 day. According to estimates based on known diffusion coefficients, this time was sufficiently long for the homogenization of the mixture. To make sure that the arene concentration calculated in terms of the partial pressures of the components in the storage bottles is equal to the actual arene concentration in the shock tube, we carried out the spectrophotometric determination of the concentrations of all of the aromatic compounds just in the shock tube for a number of working mixtures. The measurements were taken at a wavelength of 204.2 nm, for which the extinction coefficients of all of the arenes are known (benzene [14], toluene [15], ethylbenzene [16]). The source of 204.2-nm light was a VS-2 germanium electrodeless ball lamp energized by a PPBL-2 microwave-frequency generator.

The table lists the working mixture compositions and the temperature and overall density ranges behind the reflected shock wave for each mixture, which were calculated under the assumption that the equilibrium between all degrees of freedom of all gas components is established instantaneously and there are no chemical reactions.

#### *Two-Beam Absorption–Emission Technique*

This technique was used to simultaneously measure the time profiles of the soot concentration and effective soot temperature behind the reflected shock wave. The relative soot concentration as the ratio of the carbon atom concentration due to the soot to the total carbon atom concentration in the system—so-called soot yield—is usually determined in practice.

**Soot yield determination.** It is assumed that light absorption by soot particles is described by Mie's theory of electrodynamics in terms of macroscopic complex refractive index independent of the soot particle size. Because the soot particle size is much smaller than the probing light wavelength  $\lambda$  [17], the beam attenuation can be described with fairly high accuracy

## Composition of the argon-based working mixtures

Aromatic compound concentration, %	Oxygen concentration, %	Temperature range, K	Range of total densities $\times 10^5$ , mol/cm <sup>3</sup>
Benzene			
0.18	—	1670–2120	1.8–2.1
0.47	—	1640–2290	2.0–2.1
0.62	—	1780–2610	2.1–2.2
0.62	0.5	1690–2250	2.0–2.2
1.00	—	1710–2680	2.1–2.4
Toluene			
0.10	—	1760–1980	1.9–1.9
0.11	—	1690–2000	1.8–2.0
0.15	—	1580–2070	1.8–2.0
0.25	—	1650–2180	1.9–2.1
0.40	—	1680–2450	2.0–2.1
0.50	—	1760–2360	1.8–2.1
0.70	—	1910–2150	2.1–2.2
0.90	—	1740–2340	2.0–2.5
Ethylbenzene			
0.33	—	1855–2320	1.6–2.1

using the Rayleigh approximation. The absorbance of soot particles will appear as

$$\ln\left(\frac{I_0}{I}\right) = l \sum \sigma_j(\lambda) n_j, \quad (1)$$

where  $l$  is the optical path length,  $\sigma_j(\lambda)$  is the absorption cross section of a soot particle containing  $j$  carbon atoms, and  $n_j$  is the concentration of such particles. Here, summation is performed over all  $j$  values observed in the system under given conditions. In the Rayleigh approximation, the absorption cross section for a spherical particle is given by the following formula [18]:

$$\sigma_j(\lambda) = \pi r_j^2 \frac{8\pi r_j}{\lambda} E(m). \quad (2)$$

The absorption function  $E(m)$  can be represented as

$$E(m) = -\operatorname{Im}\left(\frac{m^2 - 1}{m^2 + 2}\right) = \frac{6kn}{(n^2 - k^2 + 2)^2 + 4k^2 n^2}, \quad (3)$$

where  $m = n - ik$  is the complex refractive index of soot ( $i$  is the imaginary unit).

Expressing the volume of a soot particle in terms of the number of its carbon atoms,

$$\frac{4}{3} \pi r_j^3 = \frac{\mu_C j}{\rho_C N_A}, \quad (4)$$

where  $\mu_C$  is the molar mass of carbon (12 g/mol),  $\rho_C$  is the soot density (1.86 g/cm<sup>3</sup>), and  $N_A$  is Avogadro's

number ( $6.023 \times 10^{23}$  molecule/mol), and substituting Eq. (4) into formula (2), we obtain

$$\sigma_j(\lambda) = \frac{6\pi\mu_C j}{\lambda\rho_C N_A} E(m). \quad (5)$$

The substitution of Eq. (5) into Eq. (1) yields

$$\ln\left(\frac{I_0}{I}\right) = \frac{6\pi\mu_C E(m)l}{\rho_C \lambda} \sum \frac{n_j j}{N_A} = \alpha E(m)l[C], \quad (6)$$

where  $[C]$  is the molar concentration (mol/cm<sup>3</sup>) of carbon atoms due to the soot particles and the parameter  $\alpha$  is defined as

$$\alpha = \frac{6\pi\mu_C}{\rho_C \lambda}. \quad (7)$$

For the wavelength used in this study,  $\lambda = 632.8$  nm, expression (7) gives  $\alpha = 1.922 \times 10^6$  cm<sup>2</sup>/mol.

Using expression (6), the soot yield (ratio of the carbon atom concentration due to the soot to the total carbon atom concentration in the system) can be represented as

$$SY = \frac{[C]}{[C]_0} = \frac{1}{\alpha l [C]_0 E(m)} \ln\left(\frac{I_0}{I}\right). \quad (8)$$

Because the  $E(m)$  values are widely scattered, for convenient analysis and comparison of our experimental data with those of other authors we first determined the product  $SY \times E(m)$ , which depends only on the observed absorbance of the soot–gas dispersion ( $\ln(I_0/I)$ ) and on the known parameters  $\alpha$ ,  $l$ , and  $[C]_0$ , as is clear from formula (8). Next, using the technique

described here, we determined  $E(m)$  and, accordingly, the absolute value of  $SY$ , which was compared with the value predicted by the model.

**Measuring the soot particle temperature.** When the characteristic rate of the thermal relaxation of particles is much higher than the characteristic rate of their heating due to exothermic surface growth reactions and than the characteristic rate of their radiative cooling, and when the intensity of radiation from chemiluminescent reactions is much lower than the intensity of the thermal radiation of the particles, the effective temperature is similar to the true gas and soot temperature. We made sure that all of these conditions were satisfied sufficiently well in our experiments.

As distinct from the conventional pyrometric technique using a single source of light (calibrated strip lamp or blackbody radiator), our experimental setup involved both an SI-10-300 calibrated strip lamp and a DKSSH-200 high-pressure xenon arc lamp. As is shown in Fig. 1, two spatially separated channels were employed, one for measuring light emission and the other for measuring light absorption. The brightness temperature of the arc lamp was  $\sim 5000$  K, which far exceeded the temperature behind the shock wave in our experiments. Therefore, the radiation from the gas in the absorption channel could be neglected. Thus, the signal that was received from this channel provided information about the true absorbance of the medium and, accordingly, about its grayness coefficient  $\varepsilon$ , which can be expressed as

$$\varepsilon = \frac{(I_0 - I)}{I_0}, \quad (9)$$

where  $I$  and  $I_0$  are the intensities of probing beam that has passed through the measurement section of the shock tube in the presence and absence of the absorbing medium, respectively.

The geometry of the emission channel was organized in such a way that the solid angles within which the emitted light propagated as it traveled to the entrance monochromator slit were equal. In this case, the signal from the calibration strip lamp ( $\Phi_{bl}$ ) and the signal from the emitting gas ( $\Phi_s$ ) in the shock tube can be represented in terms of Wien's law (since, for visible radiation,  $h\nu/k \gg T_\lambda$ ):

$$\Phi_{bl} = A \exp\left(-\frac{h\nu}{kT_\lambda}\right), \quad (10)$$

$$\Phi_s = A\varepsilon \exp\left(-\frac{h\nu}{kT_s}\right), \quad (11)$$

where  $A$  is the implementation factor depending on the parameters of the measurement system (geometry, amplification factors of the photomultipliers, sensitivity of the oscilloscopes, etc.),  $h\nu$  is the energy of a quantum of the recorded radiation,  $k$  is the Boltzmann constant,  $T_\lambda$  is the brightness temperature of the strip lamp at the wavelength  $\lambda$ , and  $T_s$  is the effective tem-

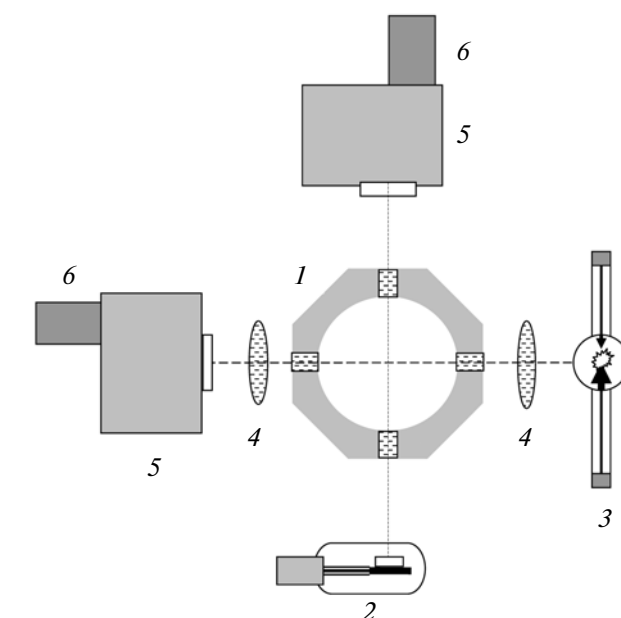


**Fig. 1.** Experimental setup for measurement of light absorption and emission by the ensemble of soot particles behind reflected shock waves: (1) shock tube, (2) tungsten strip lamp (SI-10-300), (3) xenon arc lamp (DKSSH-200), (4) lenses, (5) monochromators (DMR-4), and (6) photomultipliers (FEU-39A).

perature of the emitting gas (true temperature in the case of thermodynamic equilibrium).

Combining expressions (9)–(11), we obtain

$$T_s = T_\lambda \left[ 1 + \frac{kT_\lambda}{h\nu} \ln \left( \frac{(I_0 - I)\Phi_{bl}}{I_0\Phi_s} \right) \right]^{-1}. \quad (12)$$

The effective temperature of condensed particles was measured at  $\lambda = 632.8$  nm. The desired spectral line was separated using a DMR-4 monochromator. The radiation sensors were FEU-39A photomultipliers. The signals from the photomultipliers were recorded with S9-8 digital oscilloscopes and were then processed using a personal computer.

The strip lamp was energized by a dc power supply specially designed in our laboratory and was calibrated against current. For  $\lambda = 632.8$  nm, the dependence of the brightness temperature of the lamp on the supply current was fitted to the relationship

$$T_\lambda, \text{ K} = 592.473 + 88.665 I - 0.7168 I^2, \quad (13)$$

where  $I$  is the current passing through the lamp (A). The brightness temperature for other wavelengths was determined based on the spectral thermal radiation coefficient of tungsten [19].

## RESULTS

Figure 2 shows typical absorption and emission oscillograms and the results of their processing—the time profile of the product of the soot yield and absorption

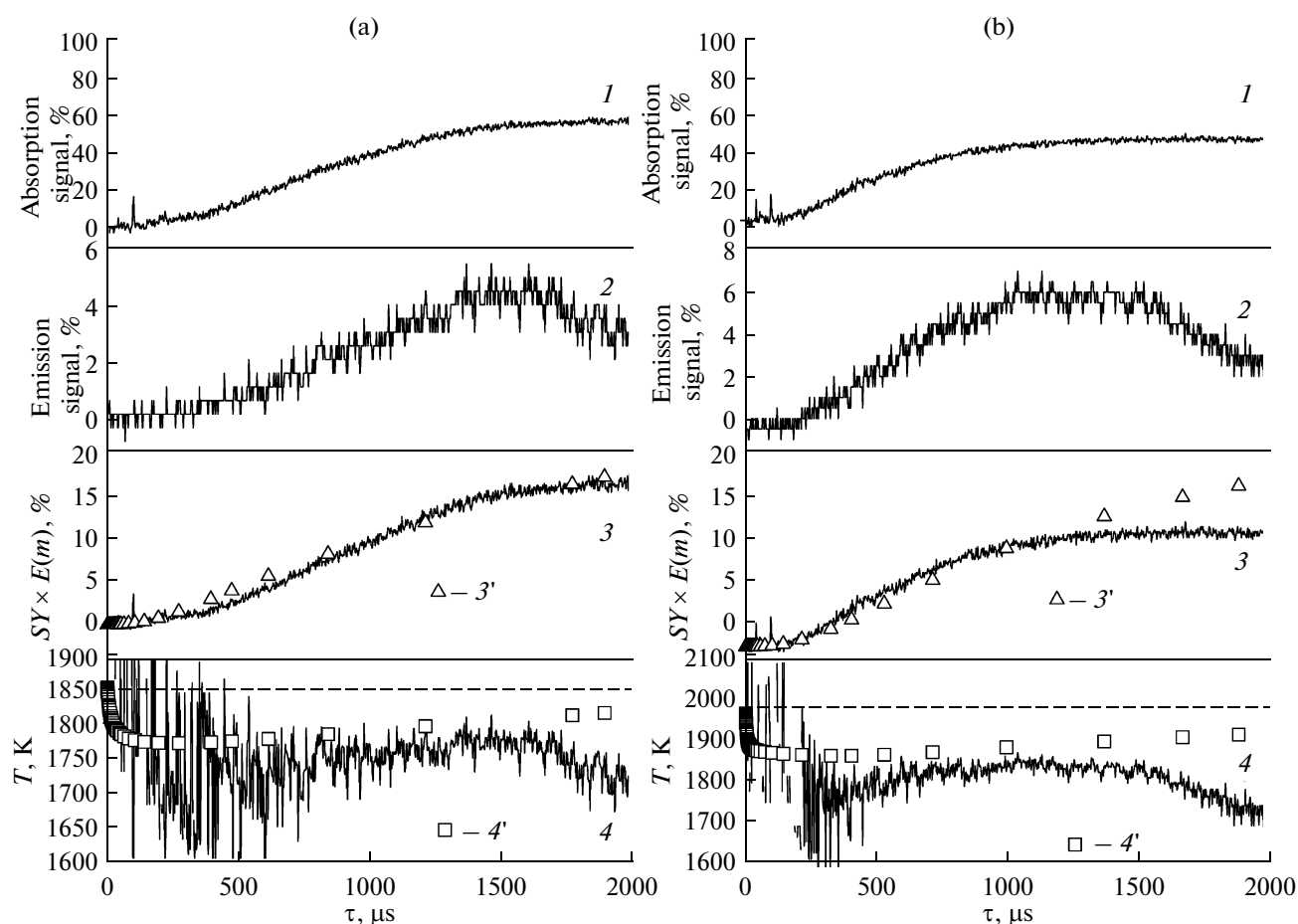


**Fig. 2.** (1, 2) Typical oscillograms of the (1) absorption and (2) emission signals as a function of time upon the arrival of the reflected shock wave front at the observation cross section and (3, 4) the time profiles of the (3) total soot yield and (4) soot particle temperature derived from the absorption and emission signals (see text) for the mixture consisting of 0.25% toluene and argon under different conditions behind the reflected shock wave: (a)  $T_{50} = 1852$  K,  $[M]_{50} = 1.96 \times 10^{-5}$  mol/cm<sup>3</sup>,  $P_{50} = 2.98$  atm; (b)  $T_{50} = 1970$  K,  $[M]_{50} = 1.93 \times 10^{-5}$  mol/cm<sup>3</sup>,  $P_{50} = 3.12$  atm. The probing wavelength is  $\lambda = 632.8$  nm. (3', 4') Calculated soot yield and soot particle temperature; (3, 4) data derived from absorption (curve 1) and emission (curves 2) signals, respectively.

function ( $SY \times E(m)$ , expression (8)) and the time profile of the soot temperature (expression (12)). Figures 3–5 present the soot yield as a function of temperature behind the shock wave (calculated under the assumption that the equilibrium between all degrees of freedom of all gas components is established instantaneously and there are no chemical reactions) for different hydrocarbon–argon mixtures. For the above-noted reasons, we initially plotted the product of the soot yield and absorption function,  $SY \times E(m)$ , not the soot yield, on the ordinate axis. Next, we determined  $E(m)$ , which allowed us to find the soot yield  $SY$ . The  $E(m)$  value was derived from the dependence of the maximum value of  $SY_{\max} \times E(m)$  as a function of temperature on the inverse carbon atom concentration ( $1/[C]_0$ ) in the toluene–argon system (Fig. 6), for which the soot yield was measured over the widest range of initial concentrations (table).

We assumed that, as the initial concentration tends to infinity, the soot yield tends to unity. This assumption is substantiated by the fact that the limiting density of the gas phase is much lower than the density of condensed matter and, therefore, at concentrations exceeding a certain threshold, the entire carbon added will pass into the condensed state (soot). Thus, an overwhelming proportion of the carbon will turn into soot; that is, at  $[C] \rightarrow \infty$ ,  $SY \rightarrow 1$ .

At the same time, it can be supposed that, at low carbon contents, the amount of soot forming in a given time interval (1 ms in our experiments) will be proportional to the soot nucleation rate and to the rate of soot particle growth via the addition of carbon-containing molecules and radicals. By analogy with classical condensation theory [20], it can be assumed that the rate of both of these processes is proportional to some power of the carbon concentration in the system.

Thus, under our experimental conditions, the amount of soot forming in a given time interval and, accordingly, the soot yield are proportional to some power of the carbon concentration. The simplest function satisfying these conditions is

$$SY_{\max} = \frac{1}{1 + a(1/[C]_0)^b} \quad (14)$$

This function was used to approximate the calculated dependence of the maximum value of the soot yield as a function of temperature on the total carbon concentration in the system. The calculations were carried out via the scheme described above. Relationship (14) was found to provide a good fit to the calculated dependence of  $SY_{\max}$  on  $[C]_0$ . This allowed us to fit experimental data (Figs. 3–5) to function (14).

It follows from the foregoing that the ordinate intercept of curve 2 in Fig. 6 indicates the  $E(m)$  value. With the 95% confidence interval on the ordinate axis (Fig. 6) taken into account,  $E(m) = 0.37 \pm 0.11$ .

This value is somewhat larger than the mean values that follow from the analyses of other authors [21–23]:  $E(m) \approx 0.3$ . At the same time,  $E(m)$  values similar to the value obtained in this study have been reported:  $E(m) \approx 0.37$  [24, 25]. Furthermore, some of the reported values are larger than our value:  $E(m) \approx 0.4$  [26] and  $E(m) \approx 0.5$  [27]. Apparently,  $E(m)$  depends on the soot formation conditions and temperature, so the value obtained under the typical experimental conditions of this study seems to be the most reliable. Note that, within the above-indicated error, our value is in agreement with many of the values reported in [21–23]. For this reason, we used the value of  $E(m) = 0.37 \pm 0.11$  in the determination of  $SY$  and in comparing it with the calculated soot yields for the three aromatic compounds examined.

## KINETIC MODEL

The kinetic mechanism of soot formation was constructed in the same way as in our previous works [10–12]. Similar principles were used in the construction of the kinetic mechanism for the high-temperature combustion of hydrocarbon fuels ranging from methane to isooctane with the formation of benzene molecules (precursors of nuclei of soot particles) taken into account [28].

In the construction of these large kinetic schemes, of particular significance is the consistency of kinetic parameters, thermodynamic data, and hypotheses involved in the model. Our kinetic model is based on the symbiosis of several kinetic mechanisms, and each of the mechanisms was tested with respect to certain groups of components [29, 30–32]. Combining dissimilar models into a single kinetic mechanism should be done very carefully because kinetic parameters and thermodynamic data for the same species and reactions may be different. The kinetic mechanism sug-

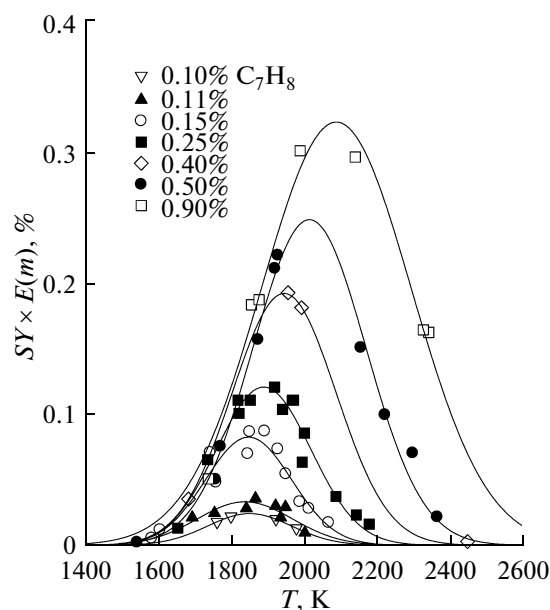


**Fig. 3.** Experimental temperature dependences of the soot yield ( $SY \times E(m)$ ) for the pyrolysis of different toluene–argon mixtures behind reflected shock waves. The toluene concentrations are specified in the legend. The solid lines are fits to experimental data points.

gested by Wang et al. [29] for lower hydrocarbons, such as methane ( $\text{CH}_4$ ) and  $\text{C}_2$ – $\text{C}_4$  hydrocarbons, was augmented by adding reactions involving  $\text{C}_5$  and  $\text{C}_7$  components [30, 31]. Reactions involving aromatic components (benzene and toluene [30, 33]) and higher alkanes ( $n$ -heptane [32]) were also included. In this augmentation of the kinetic mechanism, we added only those reactions and components which were missing in our mechanism. Although this approach cannot ensure the absolute consistency of all kinetic parameters of the model, the new kinetic model will obviously have a higher predictive power. The rate constants in the new kinetic mechanism were not varied in order to attain better agreement with experimental data.

Because the new mechanism included components and reactions involved in less general reaction mechanisms, the kinetic scheme had to be constructed very thoroughly and carefully. In doing this, we adhered to the following rules: if any component or reaction is missing in the old mechanism, simply add it to this mechanism; if identical reactions appear in the new mechanism, prefer the reaction that is present in the old mechanism. The novelty of the kinetic mechanism used in this study is that the main block of reactions involved in our old mechanism, taken from a work by Appel et al. [34], is entirely replaced with the mechanism developed recently by Wang et al. [29]. Thermodynamic data have also been revised significantly, so that the new mechanism is based on the data reported

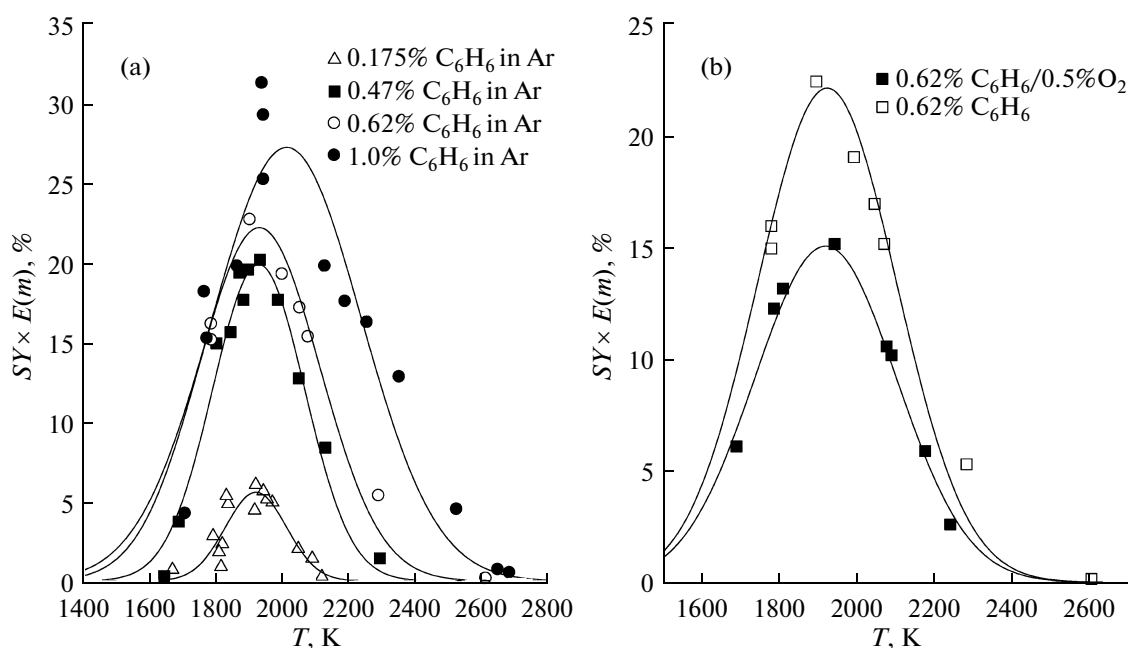


**Fig. 4.** Experimental temperature dependences of the soot yield ( $SY \times E(m)$ ) for the pyrolysis of (a) benzene–argon and (b) benzene–argon–oxygen mixtures behind reflected shock waves. The solid lines are fits to experimental data points.

by Wang et al. [29]. For the species that are missing in the reaction mechanism and in the thermodynamic data file of Wang et al. [29], thermodynamic data were taken from other reaction mechanisms [30–32] that were included as components in our complete reaction mechanism.

The mechanism of Wang et al. [29] comprises a number of new reaction routes, including those involving vinylidene. Nevertheless, we augmented this mechanism with a variety of extra reaction channels of formation and growth of polyaromatic hydrocarbon molecules (up to coronene) and with a number reactions involving  $C_3$ ,  $C_5$ , and  $C_7$  hydrocarbons [30, 31]. In particular, the new mechanism includes the following reactions: (1) consecutive growth of polyaromatic hydrocarbon molecules via the H abstraction/ $C_2H_2$  addition (HACA) mechanism, (2) combination of phenyl radicals with benzene ( $C_6H_6$ ) molecules, (3) cyclopentadienyl recombination, and (4) ring closure reactions of higher aliphatic hydrocarbons.

In view of the importance of alkyl peroxide chemistry at low and medium temperatures, we introduced reactions involving methyl peroxide ( $CH_3O_2$ ), ethyl peroxide ( $C_2H_5O_2$ ), and propyl peroxide ( $C_3H_7O_2$ ) in order to correctly account for the ignition delay in the  $CH_4/O_2/Ar$  mixtures and for the promoting effect of propane on the ignition of methane-containing mixtures [35].

The complete modified mechanism of the gas-phase reactions comprises 3320 forward and reverse reactions involving 274 components. The rate con-

stants of a number of significant reactions are presented as their pressure dependence.

According to our soot formation model, soot nuclei are polyaromatic structures resulting from addition reactions of small polyaromatic molecules (consisting of two or three aromatic rings) with small polyaromatic radicals or only from the combination of small polyaromatic radicals. The reactions yielding soot nuclei are assumed to be irreversible. It is postulated that the surface growth of the soot nuclei takes place on active sites that result from hydrogen atom abstraction by hydrogen atoms from the gas phase. Thus, two types of nuclei ensembles are considered: one involves active sites, and the other does not.

Altogether, there are three ensembles of species in our kinetic model of soot formation: active nuclei capable of further growth, inactive nuclei (i.e., nuclei without active sites), and soot particles. The distinction between these species is a matter of convention. Once we gain more detailed data as to the stage (size) at which the nuclei turn into soot particles, we will be able to improve our model. In the case considered here, this conversion is associated with the appearance of particles absorbing probing light at  $\lambda = 632.8$  nm. In our kinetic model of soot formation, the reactions in which soot nuclei form from gas-phase aromatic components are assumed to be irreversible. It is, therefore, significant to assign a right value to the rate of conversion of soot nuclei into soot particles so as to attain the best fit between the calculated and observed time profiles of the soot yield. At the nucleus-to-particle con-

version rate selected for our model, there is no nuclei accumulation in the system. Kinetically, the soot nuclei and soot particles in our model differ in that only active nuclei can be involved in growth reactions (two distinct ensembles of nuclei are considered). However, it should be taken into account that the soot particles that have a much more developed surface than the nuclei (which are essentially large molecules) are activated and deactivated by gas-phase products at a very high rate. Therefore, from the standpoint of activation and deactivation, all soot particles with a developed surface are in dynamic equilibrium. For soot particles it is, therefore, possible to consider surface growth processes with some effective rate constants. The surface growth of soot particles is due to the dynamic fluxes of species that activate the surface, deactivate it, and ensure soot deposition on active sites. Note also that the contribution from the soot nuclei to the total soot yield is small, but the behavior of the nuclei in the reacting system is significant for describing the soot formation kinetics.

We investigated two approaches to the description of the surface growth of soot particles, namely, soot particle growth via the surface HACA mechanism [36] and the surface growth model suggested by Harris and Weiner [37].

The HACA mechanism of surface growth is based on the postulate that the high-temperature surface growth of carbon-containing particles of any type, including soot particles, takes place via the abstraction of a hydrogen atom followed by the addition of an acetylene molecule to the resulting active site. Note that the hydrogen atom abstraction from the surface is mainly due to the reactions of surface hydrogen atoms with hydrogen atoms from the gas phase. Thus, according to this surface growth model, there is a direct correlation between the surface growth rate and the elemental composition of the gas phase at any point in time. To improve the fit between the experimental and calculated time profiles of the soot yield, the relationship for the surface area fraction that is accessible to activating species and can participate in further growth ( $\alpha$ ), which was obtained as a complicated function of temperature and particle size for flame conditions [34], should be adapted for the shock tube conditions. This aspect needs detailed investigation.

Harris and Weiner's model of the surface growth of soot particles is based on the following assumptions: (1) surface growth takes place on active sites, such as surface defects, edges, and steps; (2) the number of active sites does not depend directly on coagulation, surface growth, or gas-phase processes—key proposition of the model; (3) the surface growth rate decreases as surface sites disappear during the annealing (graphitization) of soot particles, which depends on the temperature. Our calculations within this surface growth model, even without graphitization taken into account, yielded very encouraging results.

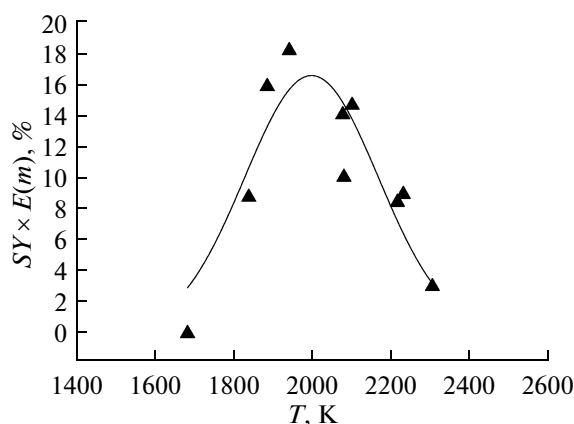


**Fig. 5.** Experimental temperature dependence of the soot yield ( $SY \times E(m)$ ) for the pyrolysis of an ethylbenzene–argon mixture (0.33%  $C_8H_{10}$  + 99.67% Ar) behind reflected shock waves ( $P_{50} = 3$  atm,  $\tau_{\text{react}} = 1$  ms). The solid lines are nonlinear-regression fits to experimental data points.

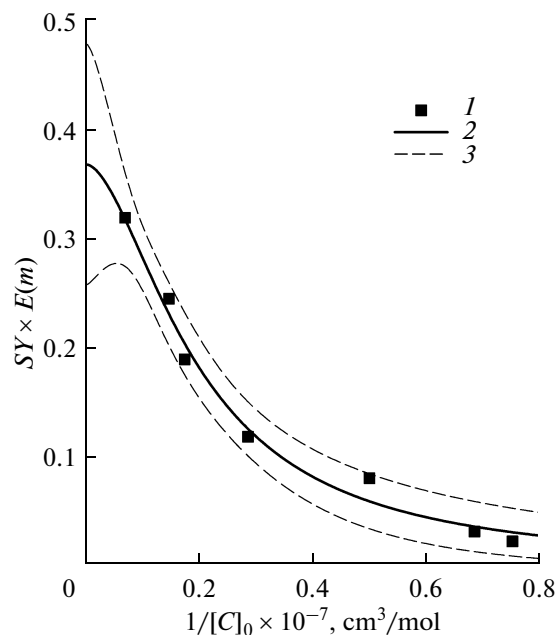


**Fig. 6.**  $SY_{\text{max}} \times E(m)$  (at  $T_{\text{max}}$ ) versus the inverse initial carbon concentration  $[C]_0$  in the system: (1) experimental data, (2) regression line corresponding to Eq. (14), and (3) 95% confidence interval. The best fit to Eq. (14) is attained at  $a = 17.2$  and  $b = 1.75$ .

Then soot formation model considered in this work is based on the gas-phase reaction mechanism describing the pyrolysis and oxidation of the initial hydrocarbons and the formation and growth of polyaromatic hydrocarbon molecules up to coronene via various reaction routes. The formation, growth, oxidation, and coagulation of soot nuclei and particles are described using the formalism of Galerkin's discrete method [38].



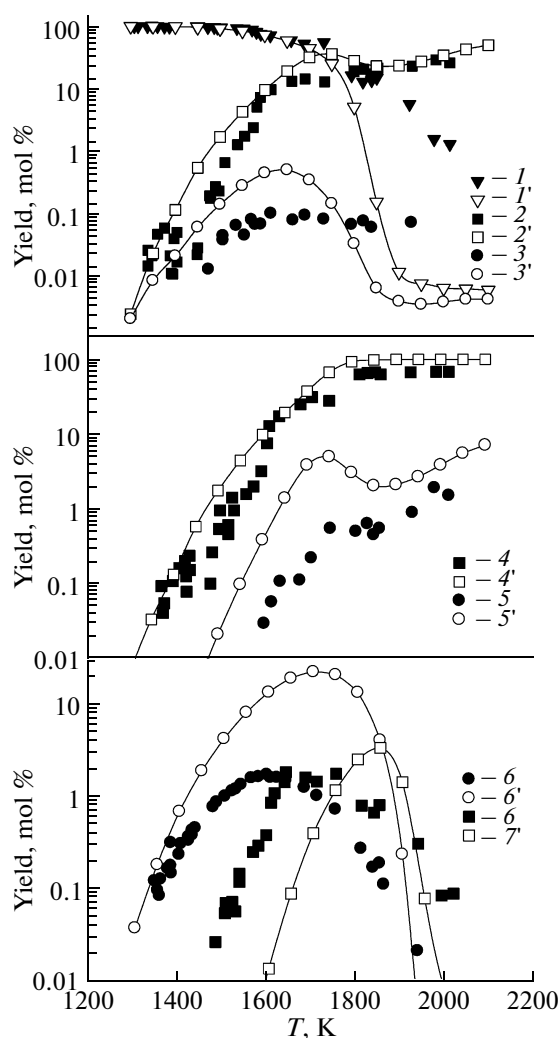


**Fig. 7.** Temperature dependences of the yields of the main products of the pyrolysis of the 0.3% benzene + argon mixture behind reflected shock waves ( $P_{50} = 50$  atm,  $\tau_{\text{react}} = 2$  ms): (1, 1')  $\text{C}_6\text{H}_6$ , (2, 2')  $\text{C}_4\text{H}_2$ , (3, 3')  $1\text{-C}_6\text{H}_4$ , (4, 4')  $\text{C}_2\text{H}_2$ , (5, 5')  $\text{C}_6\text{H}_2$ , (6, 6')  $\text{C}_6\text{H}_5\text{-CCH}$ , and (7, 7')  $\text{C}_6\text{H}_5\text{-C}_6\text{H}_5$ . (1–7) Experimental data [49]; (1'–7', lines) results of our kinetic calculations.

In our soot formation model, soot nuclei form via radical–molecule reactions involving various polyaromatic hydrocarbons ranging from phenylacetylene, acenaphthylene, and ethenylnaphthalene to coronene, as well as via radical–radical reactions, with radicals ranging from cyclopentaphenanthrenyl to coronenyl. These reactions yield polyaromatic molecules containing 16 to 48 carbon atoms. These molecules are stabilized through the formation of new chemical bonds. Soot nuclei are activated via their reactions with H and  $\text{OH}^\bullet$  radicals and are deactivated by reaching with H,  $\text{H}_2$ , and  $\text{H}_2\text{O}$ . The activated soot nuclei grow by adding  $\text{C}_2\text{H}_2$ ,  $\text{C}_4\text{H}_2$ , and  $\text{C}_6\text{H}_2$  molecules from the gas phase (the concentration of these species is rather high in the pyrolysis and oxidation of

rich mixtures containing aliphatic and aromatic hydrocarbons), by reacting with polyaromatic molecules and radicals, and by interacting with one another (coagulation). The soot nuclei are oxidized by O and  $\text{OH}^\bullet$ . The nuclei turn into soot particles via internal conversion, without involving the gas phase. The soot particles grow by adding molecules of aliphatic hydrocarbons ( $\text{C}_2\text{H}_2$ ,  $\text{C}_4\text{H}_2$ ,  $\text{C}_6\text{H}_2$ ) and polyaromatic hydrocarbons and radicals. The soot particles undergo coagulation. The oxidation of the soot particles is due to their reactions with O and  $\text{OH}^\bullet$  [10].

The basic distinction between the gas-phase reaction mechanism considered in this work and our earlier mechanism [41, 42] is that the new mechanism includes a new block of ethylene and acetylene combustion reactions that has recently been developed by Wang et al. [29], as well as a new block of polyene hydration reactions resulting in the cleavage of higher polyene molecules and in the formation of smaller hydrocarbon molecules [33, 39]. The higher polyynes ( $\text{C}_{10}\text{H}_2$  and  $\text{C}_{12}\text{H}_2$ ) were excluded from the reaction network. Taking into account earlier experimental data [40], we excluded the block of polyene condensation reactions yielding soot nuclei [41, 42] from the new soot formation model.

## DISCUSSION

The new kinetic model was thoroughly tested. We calculated the time profiles for the concentrations of hydrogen atoms resulting from the pyrolysis of benzene [43] and phenol [44] in a shock tube,  $\text{OH}^\bullet$  radicals resulting from the oxidation of toluene and *n*-heptane behind the reflected shock front [45], and methyl radicals resulting from the thermal decomposition of ethylene in a shock tube [46]. Comparison between the calculated and experimental profiles demonstrated that they are in satisfactory agreement and that the data calculated in this study differ only slightly from the calculated data presented in our previous work [10]. We also compared the calculated and measured yields of the main products forming in the gas phase in the shock-tube pyrolysis of toluene–neon [47], benzene–neon [48], benzene–argon [49], methane–argon (2.0%  $\text{CH}_4/\text{Ar}$  and 5.0%  $\text{CH}_4/\text{Ar}$ ) [50], and propane–argon (1.6%  $\text{C}_3\text{H}_8/\text{Ar}$ ) [51] mixtures. As is clear from Figs. 7–9, the new kinetic model provides a rather good description for the time variation of the yields of the main components forming in the gas phase in the pyrolysis of toluene and benzene in neon and argon.

As can be seen from Fig. 7, the calculated temperature dependences of the yields of the main products of 0.3%  $\text{C}_6\text{H}_6/\text{Ar}$  pyrolysis in reflected shock waves ( $P_{50} = 5$  atm,  $\tau_{\text{react}} = 2$  ms) are in good agreement with the experimental dependences [49]. Note the wide temperature interval (1300–2000 K) in which benzene pyrolysis was studied experimentally and our calcula-

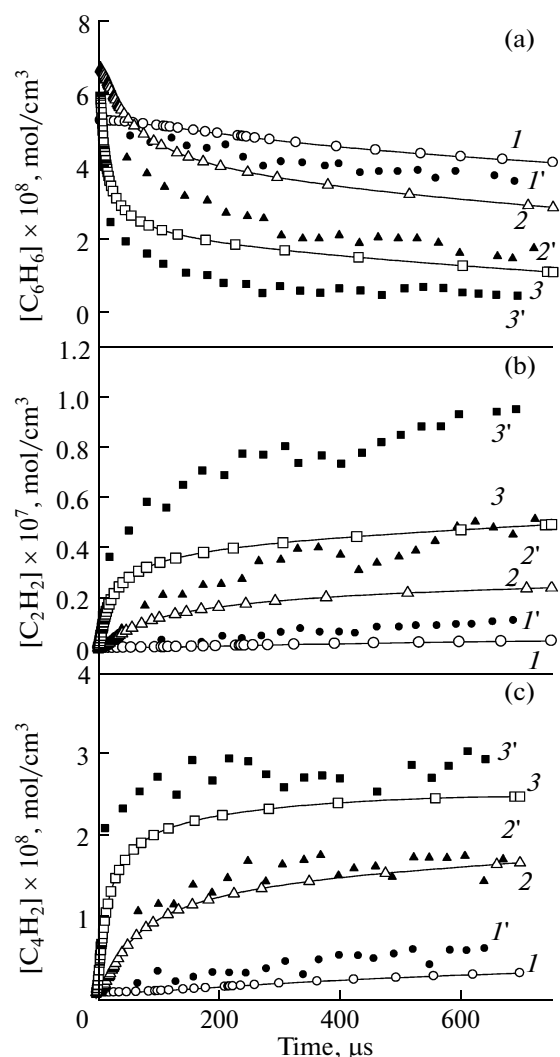


**Fig. 8.** Time profiles of the concentrations of the major products forming in the gas in the pyrolysis of the 2.1%  $C_6H_6/Ne$  mixture behind reflected shock waves [48] for three different temperatures and pressures: (a) benzene  $C_6H_6$ ; (b) acetylene  $C_2H_2$ ; (c) diacetylene  $C_4H_2$ ; (1, 1')  $T_{50} = 1704$  K,  $P_{50} = 0.36$  atm; (2, 2')  $T_{50} = 1942$  K,  $P_{50} = 0.52$  atm; (3, 3')  $T_{50} = 2192$  K,  $P_{50} = 0.52$  atm. (1–3) Our calculated data; (1'–3') experimental data [48].

tions of the molar percentages of the main pyrolysis products— $C_6H_6$ ,  $C_2H_2$ ,  $C_4H_2$ ,  $C_6H_2$ , 1- $C_6H_4$  (hex-3-ene-1,5-diyne),  $C_6H_5C_2H$  (phenylacetylene), and biphenyl—were carried out.

Figures 8 and 9 present the time profiles of the concentrations of the main products forming in the gas phase in the pyrolysis of the 2.1%  $C_6H_6/Ne$  mixtures behind reflected shock waves (benzene  $C_6H_6$ , acetylene  $C_2H_2$ , and diacetylene  $C_4H_2$ ) for three different temperatures and pressures and the time profiles of the main products forming in the gas phase in the pyrolysis of the 1.8% toluene/neon mixture behind reflected shock waves at  $T_{50} = 1900$  K and  $P_{50} = 0.4$  atm. Clearly,

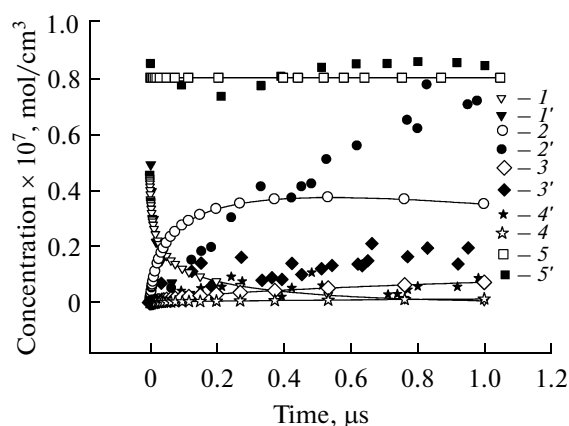


**Fig. 9.** Time profiles of the concentrations of the major products forming in the gas in the pyrolysis of the 1.8% toluene–neon mixture behind reflected shock waves [47] at  $T_{50} = 1900$  K and  $P_{50} = 0.4$  atm: (1, 1') toluene; (2, 2') acetylene  $C_2H_2$ ; (3, 3') diacetylene  $C_4H_2$ ; (4, 4') triacylene  $C_6H_2$ ; (5, 5')  $C_{total}/4$ , where  $C_{total}$  is the total carbon atom concentration in the initial mixture. (1–5) Our calculated data; (1'–5') experimental data [47].

the calculated and experimental data are in good agreement.

The calculated data were also compared with our experimental data for soot formation in the pyrolysis of aromatic hydrocarbon–argon mixtures in reflected shock waves: toluene/Ar (Fig. 10), benzene/Ar and benzene/ $O_2$ /Ar (Fig. 11), and ethylbenzene/Ar (Fig. 12). Clearly, the experimental and calculated temperature dependences of the soot yield for benzene–, toluene–, and ethylbenzene–argon mixtures practically coincide.

As the hydrocarbon concentration in the mixture is raised, the soot yield maximum shifts to higher temperatures (Figs. 3, 4). The results of kinetic calculations show the same trend (Figs. 10, 11). The time profile of the particle temperature (which is actually the gas temperature) in the pyrolysis of the aromatic hydrocarbons examined in this study, determined by optical measurements of the absorption and emission of the ensemble of soot particles formed behind the reflected shock wave front, has the following specific features. Immediately behind the reflected shock wave front, the temperature decreases appreciably because of the fragmentation of the initial hydrocarbon and, possibly, intermediate products. The temperature drop increases with an increasing hydrocarbon percentage in the mixture because of the increasing energy consumption in the fragmentation processes. Thereafter, the temperature remains nearly invariable for some time and then increases slightly. After the rarefaction wave arrives at the measurement cross section of the shock tube (in  $\sim 1500$   $\mu s$ ), the emission signals from the ensemble of soot particles begin to decrease markedly. This likely indicates a decrease in the mixture temperature in this cross section. The absorption sig-

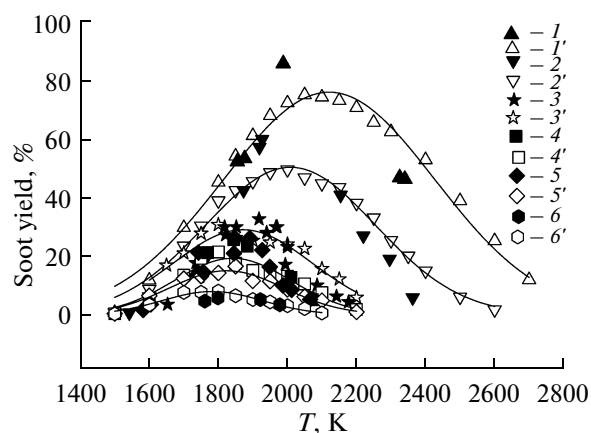


**Fig. 10.** Temperature dependences of the experimental and calculated soot yields for the pyrolysis of toluene–argon mixtures: (1, 1') 0.9%  $C_7H_8/Ar$ , (2, 2') 0.5%  $C_7H_8/Ar$ , (3, 3') 0.25%  $C_7H_8/Ar$ , (4, 4') 0.17%  $C_7H_8/Ar$ , (5, 5') 0.15%  $C_7H_8/Ar$ , and (6, 6') 0.097%  $C_7H_8/Ar$ ;  $P_{50} = 3.0$  atm;  $\tau_{\text{react}} = 1$  ms. (1–6) Our experimental data with  $E(m) = 0.37$ ; (1'–6') results of our kinetic calculations.

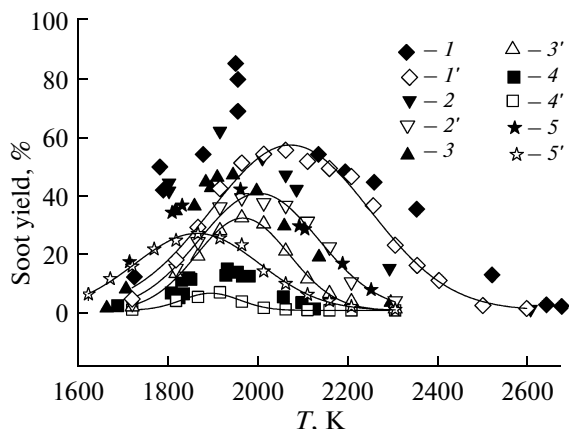


**Fig. 11.** Temperature dependences of the soot yield for the pyrolysis of benzene–argon mixtures in reflected shock waves: (1, 1') 1.0%  $C_6H_6/Ar$ , (2, 2') 0.62%  $C_6H_6/Ar$ , (3, 3') 0.467%  $C_6H_6/Ar$ , (4, 4') 0.175%  $C_6H_6/Ar$ , and (5, 5') 0.62%  $C_6H_6/0.5\% O_2/Ar$ ;  $P_{50} = 3.0$  atm;  $\tau_{\text{react}} = 1$  ms. (1–5) Our experimental data; (1'–5') results of our kinetic calculations; the solid lines are nonlinear-regression fits to the calculated kinetic data.

nals are much less sensitive to temperature variations at the late stages of soot formation because the most significant rapid processes—nucleation and surface growth of soot particles—are ended by this time. As is clear from Fig. 2, the experimental temperature and soot yield profiles behind the reflected shock wave front are fairly similar to the calculated profiles. Therefore, temperature variation behind the reflected shock wave front in the pyrolysis of the hydrocarbons examined is the major factor causing the shift of the soot yield maximum to higher temperatures.

Since the temperature behind the shock front varies with time in a complicated way (rapid fall to a

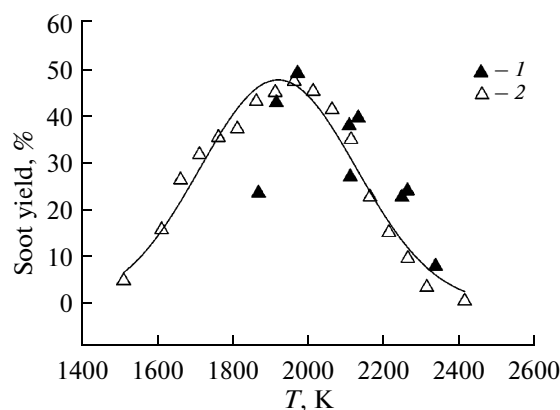


**Fig. 12.** Temperature dependence of the soot yield for the pyrolysis of an ethylbenzene–argon mixture (0.33%  $C_8H_{10} + 99.67\% Ar$ ) in reflected shock waves:  $P_{50} = 3.0$  atm;  $\tau_{\text{react}} = 1$  ms; (1) our experimental data; (2) results of our kinetic calculations; the solid lines are nonlinear-regression fits to the calculated kinetic data.

quasi-steady-state value, growth, and a new decrease upon the arrival of the rarefaction wave), the ultimate soot yield is determined by the entire temperature profile, not only by the quasi-steady-state temperature. In addition, all kinetic calculations were performed for nonisothermal conditions and a constant density, and the calculated kinetic data are in good agreement with the corresponding experimental data. For this reason, we did not adjust our experimental data points to some “effective temperature” behind the reflected shock wave and used the initial temperature  $T_{50}$  both in the representation of experimental data and in the calculations.

The introduction of oxygen into the system causes a systematic increase in the temperature of the reaction mixture and a decrease in the temperature immediately behind the reflected shock wave front. This shifts the soot yield maximum to lower temperatures (Fig. 11).

As is clear from the above results, the new kinetic model of soot formation quite satisfactorily reproduces experimental soot yield data for the pyrolysis of aromatic hydrocarbons in a wide temperature range.

An analysis of reaction routes and an analysis of the sensitivity of the calculated kinetic data to variations of the rate constants of elementary reactions of the kinetic mechanism make up an independent, rather complicated, and rather laborious problem, considering the great number of reactions involved in the kinetic scheme, so this problem will be the subject of a separate study.

## CONCLUSIONS

Thus, we gained some new experimental data on the basic parameters of soot formation in the pyrolysis

and oxidative pyrolysis of aromatic hydrocarbons in reflected shock waves. These data prompted us to thoroughly analyze, augment, and modify our previous detailed kinetic model of soot formation. The new kinetic model of soot formation reproduces the time dependences reported by other authors for the concentrations of some key components forming at the early stages of the pyrolysis and oxidation of hydrocarbons in wide ranges of experimental conditions. In our simulation of soot formation, the new model reproduces well the observed time dependences of the soot yield and particle temperature for the pyrolysis of a number of aromatic hydrocarbons (benzene, toluene, ethylbenzene) behind reflected shock waves.

Soot formation in hydrocarbon pyrolysis and oxidation is accompanied by a considerable temperature drop immediately behind the reflected shock wave front. This is likely due to the dominating effect of the heat of decomposition of various hydrocarbon species and fragments. This temperature drop is somewhat smaller in the presence of oxygen in the reacting mixture owing to the effect of exothermic oxidation reactions, and this observation is also predicted by the new kinetic model.

#### ACKNOWLEDGMENTS

This work was carried out in the framework of the Federal Target Program "Scientific and Scientific-Pedagogical Personnel of Innovative Russia" (state contract NK-576P) and was supported by the Russian Foundation for Basic Research (project no. 08-08-00722-a).

#### REFERENCES

1. Frenklach, M., *Phys. Chem. Chem. Phys.*, 2002, vol. 4, p. 2028.
2. Whitesides, R. and Frenklach, M., *J. Phys. Chem. A*, 2010, vol. 114, p. 689.
3. D'Anna, A., in *Combustion Generated Fine Carbonaceous Particles*, Bockhorn, H., D'Anna, A., Sarofim, A.F., and Wang, H., Eds., Karlsruhe: KIT, 2009, p. 289.
4. D'Anna, A., Violi, A., D'Alessio, A., and Sarofim, A.F., *Combust. Flame*, 2001, vol. 127, p. 1995.
5. Violi, A., Sarofim, A.F., and Truong, T.N., *Combust. Sci. Technol.*, 2002, vol. 174, p. 205.
6. Violi, A., *Combust. Flame*, 2004, vol. 139, p. 279.
7. Chung, S.H. and Violi, A., in *Combustion Generated Fine Carbonaceous Particles*, Bockhorn, H., D'Anna, A., Sarofim, A.F., and Wang, H., Eds., Karlsruhe: KIT Scientific, 2009, p. 321.
8. Öktem, B., Tolocka, M.P., Zhao, B., Wang, H., and Johnston, M.V., *Combust. Flame*, 2005, vol. 142, p. 364.
9. Baquet, T.G., Grotheer, H., and Aigner, M., *Rapid Commun. Mass Spectrom.*, 2007, vol. 21, p. 4060.
10. Agafonov, G.L., Naydenova, I., Vlasov, P.A., and Warnatz, J., *Proc. Combust. Inst.*, 2007, vol. 31, p. 575.
11. Agafonov, G.L., Borisov, A.A., Smirnov, V.N., Troshin, K.Ya., Vlasov, P.A., and Warnatz, J., *Combust. Sci. Technol.*, 2008, vol. 180, p. 1876.
12. Agafonov, G.L., Naydenova, I., Smirnov, V.N., Vlasov, P.A., and Warnatz, J., in *Combustion Generated Fine Carbonaceous Particles*, Bockhorn, H., D'Anna, A., Sarofim, A.F., and Wang, H., Eds., Karlsruhe: KIT Scientific, 2009, p. 385.
13. Stupochenko, E.V., Losev, S.A., and Osipov, A.I., *Relaksatsionnye protsessy v udarnykh volnakh* (Relaxation Processes in Shock Waves), Moscow: Nauka, 1965.
14. Feng, R., Cooper, G., and Brion, C.E., *J. Electron. Spectrosc. Relat. Phenom.*, 2002, vol. 123, p. 199.
15. Hippler, H., Troe, J., and Wendelken, H.J., *J. Chem. Phys.*, 1983, vol. 78, p. 5351.
16. Brouwer, L., Muller-Markgraf, W., and Troe, J., *Ber. Bunsen Ges. Phys. Chem.*, 1983, vol. 87, p. 1031.
17. Haynes, B.S. and Wagner, H.Gg., *Prog. Energy Combust. Sci.*, 1981, vol. 7, no. 4, p. 229.
18. Van de Hulst, H.C., *Light Scattering by Small Particles*, New York: Dover, 1981.
19. *Fizicheskie velichiny. Spravochnik* (Physical Quantities: A Handbook), Grigor'ev, I.S. and Meilikhov, E.Z., Eds., Moscow: Energoatomizdat, 1991, p. 779.
20. Frenkel, Ya.I., *Kineticheskaya teoriya zhidkosti* (Kinetic Theory of the Liquid), Moscow: Akad. Nauk SSSR, 1946.
21. Bond, T.C. and Bergstrom, R.W., *Aerosol Sci. Technol.*, 2006, vol. 40, p. 27.
22. Schulz, C., Kock, B.F., Hofmann, M., Michelsen, H.A., Will, S., Bougie, B., Suntz, R., and Smallwood, G., *Appl. Phys. B*, 2006, vol. 83, p. 333.
23. Michelsen, H.A., Schrader, P.E., and Goulay, F., *Carbon*, 2010, vol. 48, no. 8, p. 2175.
24. Williams, T.C., Shaddix, C.R., Jensen, K.A., and Suo-Anttila, J.M., *Int. J. Heat Mass Transfer*, 2007, vol. 50, nos. 7–8, p. 1616.
25. Schnaiter, M., Horvath, H., Mohler, O., Naumann, K.H., Saathoff, H., and Schock, O.W., *J. Aerosol Sci.*, 2003, vol. 34, p. 1421.
26. Beyer, V. and Greenhalgh, D.A., *Appl. Phys. B*, 2006, vol. 83, p. 455.
27. Erickson, W.D., Williams, G.C., and Hottel, H.C., *Combust. Flame*, 1964, vol. 8, p. 127.
28. Blanquart, G., Pepiot-Desjardins, P., and Pitsch, H., *Combust. Flame*, 2009, vol. 156, p. 588.
29. Wang, H., You, X., Joshi, A.V., Davis, S.G., Laskin, A., Egolfopoulos, F., and Law, C.K., *USC Mech Version II, High-Temperature Combustion Reaction Model of H<sub>2</sub>/CO/CI–C<sub>4</sub> Compounds*, available from [http://ignis.usc.edu/USC\\_Mech\\_II.htm](http://ignis.usc.edu/USC_Mech_II.htm), May 2007.
30. Richter, H., Granata, S., Green, W.H., and Howard, J.B., *Proc. Combust. Inst.*, 2005, vol. 30, p. 1397.
31. Skjøth-Rasmussen, M.S., Glarborg, P., Østberg, M., Johannessen, J.T., Livbjerg, H., Jensen, A.D., and Christensen, T.S., *Combust. Flame*, 2004, vol. 136, p. 91.
32. Correa, C., Niemann, H., Schramm, B., and Warnatz, J., *Proc. Combust. Inst.*, 2000, vol. 28, p. 1607.

33. Frenklach, M. and Warnatz, J., *Combust. Sci. Technol.*, 1987, vol. 51, p. 265.
34. Appel, J., Bockhorn, H., and Frenklach, M., *Combust. Flame*, 2000, vol. 121, p. 122.
35. Huang, J. and Bushe, W.K., *Combust. Flame*, 2006, vol. 144, p. 74.
36. Frenklach, M. and Wang, H., in *Soot Formation in Combustion*, Bockhorn, H., Ed., Berlin: Springer, 1994, p. 162.
37. Harris, S.J. and Weiner, A.M., *Combust. Sci. Technol.*, 1983, vol. 31, p. 155.
38. Deuflhard, P. and Wulkow, M., *Impact Comput. Sci. Eng.*, 1989, vol. 1, p. 269.
39. Frenklach, M., Clary, D.W., Yuan, T., Gardiner, W.C., Jr., and Stein, S.E., *Combust. Sci. Technol.*, 1986, vol. 50, p. 79.
40. Böhm, H. and Jander, H., *Phys. Chem. Chem. Phys.*, 1999, vol. 1, p. 3775.
41. Vlasov, P.A. and Warnatz, J., *Proc. Combust. Inst.*, 2002, vol. 29, p. 2335.
42. Naydenova, I., Nullmeier, M., Warnatz, J., and Vlasov, P.A., *Combust. Sci. Technol.*, 2004, vol. 176, p. 1667.
43. Scherer, S., *PhD Dissertation*, Stuttgart: Universität Stuttgart, Institut für Physikalische Chemie der Verbrennung des DLR, 2001.
44. Horn, C. and Frank, P., *Proc. 4th Int. Conf. on Chemical Kinetics*, Gaithersburg, Md., 1997.
45. Vasudevan, V., Davidson, D.F., and Hanson, R.K., *Proc. Combust. Inst.*, 2005, vol. 30, p. 1155.
46. Oehlschlaeger, M.A., Davidson, D.F., and Hanson, R.K., *J. Quant. Spectrosc. Radiat. Transfer*, 2005, vol. 92, p. 393.
47. Kern, R.D., Singh, H.J., Esslinger, M.A., and Winkeler, P.W., *Proc. Combust. Inst.*, 1982, vol. 19, p. 1351.
48. Kern, R.D., Wu, C.H., Skinner, G.B., Rao, V.S., Kiefer, J.H., Towers, J.A., and Mizerka, L.J., *Proc. Combust. Inst.*, 1984, vol. 20, p. 789.
49. Laskin, A. and Lifshitz, A., *Proc. Combust. Inst.*, 1996, vol. 26, p. 669.
50. Hidaka, Y., Nakamura, T., Tanaka, H., Inami, K., and Kawano, H., *Int. J. Chem. Kinet.*, 1990, vol. 22, p. 701.
51. Lifshitz, A. and Frenklach, M., *J. Phys. Chem.*, 1975, vol. 79, p. 686.